

The Physics of Flash (Supernova) Spectroscopy

C. S. Kochanek^{1,2}

¹ *Department of Astronomy, The Ohio State University, 140 West 18th Avenue, Columbus OH 43210*

² *Center for Cosmology and AstroParticle Physics, The Ohio State University, 191 W. Woodruff Avenue, Columbus OH 43210*

27 July 2018

ABSTRACT

We examine flash spectroscopy of a circumstellar medium (CSM) ionized by the hard radiation pulse produced by the emerging shock of a supernova (SN). We first find that the rise and fall times of the $H\alpha$ emission constrains the location of the CSM with a peak at $t_{peak} \simeq R_* \sqrt{2/cv_s}$ for a star of radius R_* and a shock velocity of v_s . The dropping temperature of the transient emission naturally reproduces the evolution of lines with different ionization energies. Second, for red supergiants (RSGs), the shock break out radiatively accelerates the CSM to produce broad, early-time line wings independent of the Thomson optical depth of the CSM. Finally, the CSM recombination rates in binaries can be dominated by a dense, cool, wind collision interface like those seen in Wolf-Rayet binaries rather than the individual stellar winds. Combining these three results, the flash spectroscopy observations of the normal Type IIP iPTF13dqy (SN 2013fs) are naturally explained by an RSG with a normal, Thomson optically thin wind in a binary with a separation of $\sim 10^4 R_\odot$ without any need for a pre-SN eruption. Similarly, the broad line wings seen for the Type IIb iPTF13ast (SN 2013cu), whose progenitors are generally yellow supergiants in binaries, are likely due to radiative acceleration of the CSM rather than a pre-existing, Wolf-Rayet-like wind.

Key words: stars: massive – supernovae: general – supernovae: individual: iPTF13dqy

1 INTRODUCTION

Some massive stars appear to know that they are about to die. They manifest their impending death through outbursts that eject significant amounts of mass shortly before a supernova (SN), where the outbursts are either seen directly (e.g., Pastorello et al. 2007, Fraser et al. 2013, Mauerhan et al. 2013, Ofek et al. 2014, Ofek et al. 2016) or inferred from evidence for a massive circumstellar medium (CSM) once the SN occurs (e.g., Gal-Yam 2012, Smith 2014). Such systems are relatively rare, and a range of theoretical models have been proposed to explain the phenomenon (e.g., Quataert & Shiode 2012, Shiode & Quataert 2014, Smith & Arnett 2014, Woosley & Heger 2015, Fuller 2017).

One means of probing the CSM is to use “flash spectroscopy” of the CSM shortly after a supernova is discovered (Gal-Yam et al. 2014, Khazov et al. 2016). The burst of ionizing photons created by the SN shock breaking out of the surface of the star flash ionizes the CSM and the properties of any narrow emission lines in spectra of the SN taken before the CSM material can either recombine or be swept up by the expanding shock probes the density and composi-

tion of the CSM. Groh (2014) and Gräfener & Vink (2016) are able to match the early time spectra using models of Wolf-Rayet stars, consistent with a CSM photoionized by a radiation from a shock break out.

The most extensive flash spectroscopy observations are for the normal Type IIP iPTF13dqy (SN 2013fs, Yaron et al. 2017). Based on the line fluxes and widths, Yaron et al. (2017) concluded that the CSM density implied a far higher mass loss rate ($\dot{M} \sim 10^{-3} M_\odot/\text{year}$) than is typical of red supergiants. Since the SN also shows no signs of strong CSM interactions (i.e., radio or X-ray emission) in its later phases, they also conclude that the dense CSM can only extend to $\lesssim 10^{15}$ cm. Yaron et al. (2017) argue that the progenitor must have experienced a short-lived, high-mass loss precursor before exploding and that such precursors must be common.

As part of our search for failed SNe forming black holes with the Large Binocular Telescope (LBT, Gerke et al. 2015, Adams et al. 2016), we also obtain high precision light curves of the progenitors to any successful SNe in the target galaxies. We have monitored four Type IIP progenitors to date, finding no evidence for variability down to levels close to the typical variability of red supergiants (Kochanek et al.

2017, Johnson et al. 2017). The absence of any visible outbursts or evidence of dust formation, which is essentially inevitable at high mass loss rates ($\gtrsim 10^{-4} M_{\odot}/\text{year}$, see, e.g., Kochanek 2011), strongly argues that outbursts from the progenitors of Type IIP SNe are in fact uncommon. This is further supported by the lack of X-ray emission from normal Type IIP SNe (e.g., Dwarkadas 2014) although there are exceptions like SN 2013ej (Chakraborti et al. 2016). One counterargument by Morozova et al. (2017) and Morozova et al. (2018) is that a period of enhanced mass loss shortly before explosion would help to explain the shapes of Type IIP light curves.

This contradiction motivated an investigation into flash spectroscopy with the goal of better understanding iPTF13dqy. We investigate three issues, each of which has general applicability, and then apply them to iPTF13dqy. In §2 we examine the time evolution of the line fluxes due to finite light travel times and recombination as the SN cools and becomes less luminous. We find that the time evolution of the lower ionization energy lines (e.g., H α) determines the location of the emitting material. In §3 we show that the radiative acceleration of the CSM by the shock break out radiation from an RSG will produce broad line wings in early-time spectra independent of the Thomson optical depth of the CSM. In §4, we show that a radiatively cooling boundary layer produced by the collision of the winds in a binary, as seen in some Wolf-Rayet binaries, can produce a high density region that mimics a high mass loss rate from a single star.

When we apply these general results to iPTF13dqy, we come to the conclusion that emission from a wind collision region provides a more natural explanation of the observations than a pre-SN eruption. The time evolution of the H α emission requires material spanning a wide range of radii that is also detached from the stellar surface. The effects of radiative acceleration mean that a Thomson optically thick CSM is no longer needed. The overall line luminosities still require denser material than a normal RSG wind, but this is naturally supplied by a cooling wind collision region. We summarize both the general and specific conclusions in §5. Two technical points are discussed in short appendices.

2 THE EVOLUTION OF THE LINE FLUXES

In this section we develop a simple model for the time evolution of the line flux from the flash ionized wind of a star and then apply it to iPTF13dqy. We assume an initial shock break out that creates an outward moving shell of ionizing radiation. We start by assuming that the photoionizing flux is high enough to maintain complete ionization and then consider the evolution as the photoionizing flux decreases. For simplicity, we consider wind densities below the point where the shock breaks out of the wind rather than the stellar surface (see, e.g., Chevalier & Irwin 2011). The expanding radiation shell instantaneously ionizes the CSM as it expands. We will consider time scales on which the finite thickness of the radiation shell can be ignored. We assume that ionizing photons produced by recombination are locally reabsorbed (case B) and the nature of the temporal evolution allows us to ignore effects such as the production of hydrogen ionizing photons by helium recombinations. In fact,

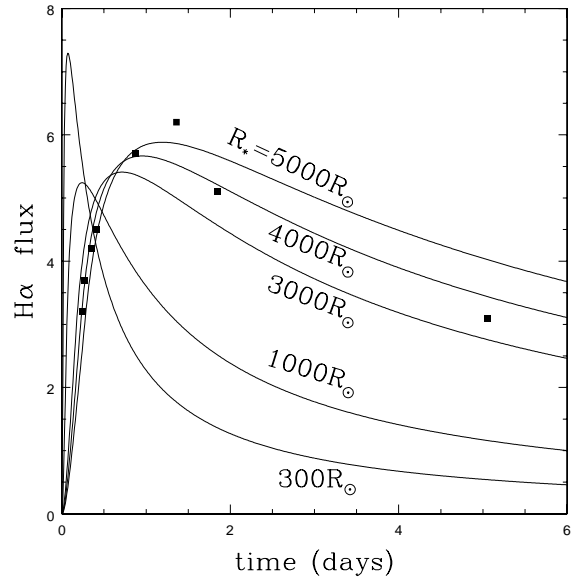


Figure 1. Recombination light curves for a wind with an inner edge at a shock radius expanding at $v_{s0} = 10^4$ km/s and an outer edge expanding at the speed of light, both starting from an initial radius of R_* . This includes the effect of light travel times but ignores any shadowing effects (Equations 11 and 12). The points are the observed H α light curve from Yaron et al. (2017) and the curves are normalized to fit the equally weighted observations. The rise time requires a stellar radius of $R_* \simeq 4000R_{\odot}$, which is not physically reasonable for a red supergiant.

for this basic analysis we will simply assume that all the electrons are due to ionized hydrogen.

We are considering a primary with radius $R_* = 1000R_{3R_{\odot}}$ and mass $M_* = 10M_{*10}M_{\odot}$ producing a $\rho \propto r^{-2}$ wind of velocity $v_w = 100v_2$ km/s and mass loss rate $\dot{M} = 10^{-4}M_4M_{\odot}/\text{year}$. For our concrete examples, we use the $15M_{\odot}$ progenitor model from Woosley et al. (2002), which has $R_* = 821R_{\odot}$ and $M_* = 12.6M_{\odot}$ when it explodes. We assume it explodes with energy $E_{SN} = 10^{51}E_{51}$ erg and has an ejecta mass of $M_e = 10M_{e10}M_{\odot}$. For our concrete example we adopt $E_{51} = 1$ and $M_e = 11.2M_{\odot}$ (i.e., forming a $1.4M_{\odot}$ neutron star).

It is useful to normalize recombination rates by the rate for an infinite wind extending from the stellar surface,

$$\Gamma_{\infty} \equiv \frac{\alpha_R \dot{M}^2}{4\pi v_w^2 \mu^2 m_p^2 R_*} \quad (1)$$

where α_R is the recombination (or a related) rate and μm_p is the relevant mean particle weight. Exactly what to use for μ depends on the ionization state of the gas. Since stellar winds generally have velocities comparable to the escape velocity of the star (e.g., Lamers & Cassinelli 1999), we can set the wind speed to be $v_w^2 = \xi 2GM_*/R_*$ where $\xi \simeq 1$ is a dimensionless number. For our fiducial model, we set $\xi = 1$, which makes $v_w = 76$ km/s. In this formulation, the recombination rate is

$$\Gamma_{\infty} = \frac{\alpha_R \dot{M}^2}{8\pi \xi \mu^2 m_p^2 GM_*} = 4.3 \frac{\alpha_{13} \dot{M}_4^2}{\xi \mu^2 M_{*10}} \times 10^{49} \text{ s}^{-1} \quad (2)$$

where $\alpha_R = 10^{-13} \alpha_{13} \text{ cm}^3/\text{s}$. Note that there is little freedom to use the wind speed to adjust the mass loss rate for

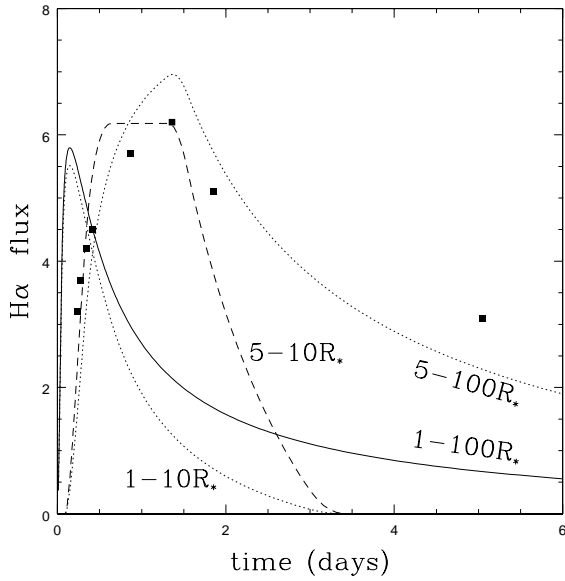


Figure 2. Recombination light curves for a $R_* = 821R_\odot$ star with a dense wind lying between $1-100R_*$ (solid). The dotted line shows the effect of truncating the wind from the outside ($1-10R_*$) or the inside ($5-100R_*$) and the dashed line shows the effect of making the wind a shell ($5-10R_*$). An inner edge of $5R_* = 4100R_\odot$ reproduces the rise in the $H\alpha$ flux well, as expected from Figure 1. The late time $H\alpha$ point requires an extended wind ($100R_* \gtrsim 6 \times 10^{15}$ cm) rather than a wind truncated on the scale of $10R_* \simeq 6 \times 10^{14}$ cm proposed by Yaron et al. (2017). The assumptions are otherwise the same as in Figure 1.

a wind arising from a stellar surface – any change in wind speed is balanced by the implied change in stellar radius. Equating Γ_∞ for Case B $H\alpha$ emission to the peak $H\alpha$ flux of iPTF13dqy (6×10^{50} $H\alpha$ photons per second) implies a mass loss rate of

$$\dot{M} \simeq 3.7\xi^{1/2} M_{*10}^{1/2} \alpha_{13}^{-1/2} \times 10^{-4} M_\odot/\text{year}. \quad (3)$$

We therefore adopt $\dot{M} = 10^{-3.5} M_\odot/\text{year}$ for our fiducial models. Yaron et al. (2017) use a rate ~ 10 times higher because they assume a much larger (stellar) radius, a point we will discuss below.

The ionized region of the wind is bounded by the expanding break out pulse and the expanding shock. If the wind is fully photoionized over the region $R_s < R < R_{bo}$, the recombination rate is

$$\frac{\Gamma(t)}{\Gamma_\infty} = \frac{R_*}{R_s} \left(1 - \frac{R_s}{R_{bo}}\right). \quad (4)$$

For the flash ionization problem, the inner and outer radii of the ionized wind vary with time. The shock break out pulse has an ionizing photon rate $Q_{bo} \gg \Gamma_\infty$ and so R_{bo} expands by the smaller of the speed of light and $v_{ion} = v_w Q_{bo} m_p M^{-1}$. For reasonable parameters, Q_{bo} is so large that $R_{bo} = R_* + ct$. It does, however, produce a finite number of ionizing photons, while an infinite $1/r^2$ wind contains an infinite number of atoms, so the ionization can only extend to some maximum radius. This is generally such a large radius that we can ignore its existence.

The expansion of the shock is more complicated. For simple models, we will simply treat the shock velocity as

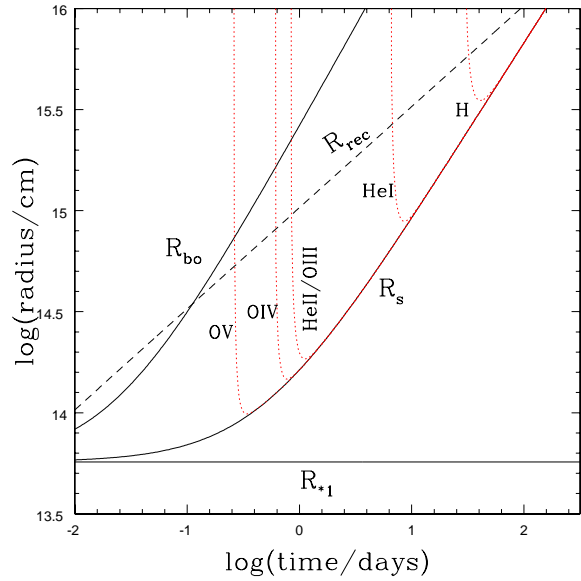


Figure 3. A space-time diagram showing the evolution of radii relevant to interpreting flash spectroscopy. A horizontal line shows the stellar radius $R_* = 821R_\odot$ chosen to match the $15M_\odot$ progenitor model of Woosley et al. (2002). $R_{bo}(t)$ shows the expansion of the ionization wave created by the shock break out radiation pulse, and $R_s(t)$ shows the expansion of the shock. The diagonal line $R_{rec}(t)$ shows the radius where the recombination time equals the elapsed time for the assumed wind properties of $\dot{M} = 10^{-3.5} M_\odot/\text{year}$ and $v_w = 76$ km/s. The curved dotted lines show, from left to right, the radii $R_{pi}(t, E_\gamma)$ to which the current rate of production of ionizing photons above E_γ can ionize OV, OIV, HeII/OIII and H. The radii plunge very rapidly due to the exponential decline of the ionizing fluxes and then turn and asymptotically track the shock radius.

a constant, $v_s = v_{s0} = 10^4 v_{s4}$ km/s. This is reasonable at early times, but at later times the shock will slow and achieve a self-similar evolution (Chevalier 1982). For this case, we adopt a shock velocity of

$$v_s = \frac{v_{s0}}{1 + (t/t_s)^{1/5}}, \quad (5)$$

which smoothly matches onto the standard self-similar solution of Chevalier (1982) while removing the divergence¹ in the velocity ($v_s \propto t^{-1/5} \rightarrow \infty$ as $t \rightarrow 0$). The time scale

$$t_s = \frac{0.6E^2 v_w}{M M_c v_0^5} = 554 \frac{E_{51}^2 v_{w2}}{M_4 M_{e10} v_{s0,4}^5} \text{ days} \quad (6)$$

is determined by matching the self-similar solution to the assumed early time shock velocity v_{s0} . Based on the initial expansion rate of the photospheric radius found by Yaron et al. (2017), $v_{s0} \simeq 20000$ km/s, so if we adopt the wind parameters from above and $E_{51} = 1$ we find that

¹ As a practical matter, we could have simply ignored the fact that the velocity diverges since the resulting radius is perfectly convergent in time. However, this formulation seemed moderately more physical and was as easy to implement. Within a few R_* of the primary, there are additional issues in any case from assuming v_w is constant in the wind acceleration region.

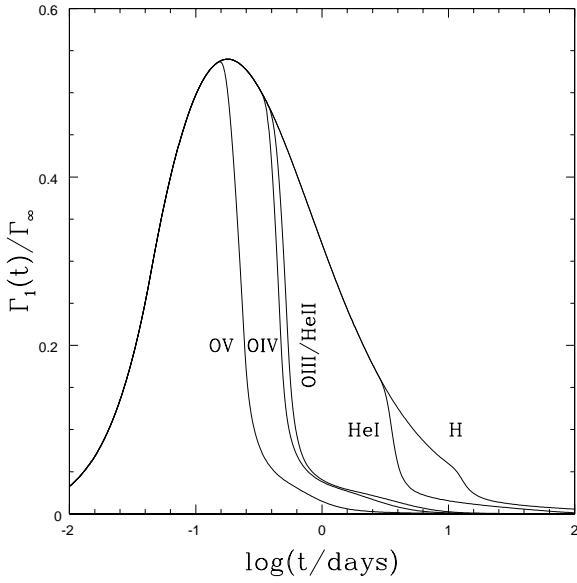


Figure 4. Recombination rates to OV, OVI, OIII/HeII, HeI and H relative to Γ_∞ as a function of time. The outer envelope is essentially the same as in Figure 1 except the shock is decelerating to follow the self-similar solution. The recombination rates collapse when the numbers of ionizing photons become too small to maintain an ionized wind. The model evolves more rapidly than iPTF13dqy because the fiducial model has $R_* = 821R_\odot$ while the data appear to require $R_* \simeq 4000R_\odot$. These are for the full numerical calculation including a slowing shock front, recombination and light propagation effects.

$t_s = 3.8$ days. The shock radius then evolves as

$$R_s(t) = R_* + \frac{5}{12} t_s v_{s0} \times \left[3\hat{t}_s^{4/5} - 4\hat{t}_s^{3/5} + 6\hat{t}_s^{2/5} - 12\hat{t}_s^{1/5} + 12 \ln(1 + \hat{t}_s^{1/5}) \right] \quad (7)$$

where $\hat{t}_s = t/t_s$. As a short hand that encompasses both solutions we can describe the shock radius as $R_s(t) = R_* + \langle v \rangle t$ where the mean velocity $\langle v \rangle$ is simply a constant or the more complex expression implied by Equation 8.

Given these definitions, Equation 4 becomes

$$\frac{\Gamma(t)}{\Gamma_\infty} = \left[1 - \frac{\langle v \rangle}{c} \right] \left[\frac{R_*}{R_* + \langle v \rangle t} \right] \left[\frac{t}{t + t_*} \right] \quad (8)$$

where $t_* = R_*/c$ is the light travel time across the star. The competition between the addition of newly ionized material by the expanding radiation front and the absorption of ionized material into the shocked layer leads to a peak in the recombination rate. For the case where $\langle v \rangle = v_{s0}$ is constant, the recombination rate peaks at

$$\frac{\Gamma_{peak}}{\Gamma_\infty} = \frac{1 - v_{s0}/c}{1 + v_{s0}/c} \quad (9)$$

when $t_{peak} = R_*/\sqrt{cv_{s0}}$. The peak recombination rate is close to that for a fully ionized wind, with $\Gamma_{peak}/\Gamma_\infty = 0.97, 0.94$ and 0.88 for $v_{s0} = 5000, 10000$ and 20000 km/s, respectively. For these same velocities, the peak occurs at $t_{peak} = 7.8, 5.5$ and $3.9t_*$.

The observer does not see this light curve because of light travel times. Light emitted at radius r and polar angle θ is delayed by $r(1 - \cos\theta)/c$ relative to emission along the

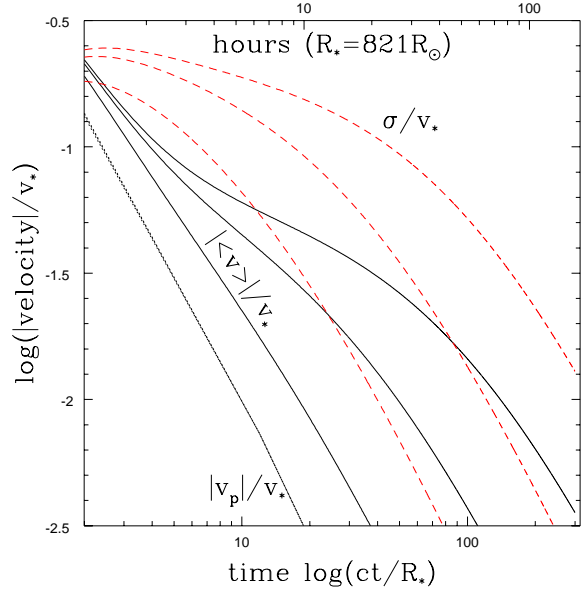


Figure 5. Evolution of the line peak velocity, $|v_p|/v_*$ (dotted), mean velocity, $\langle v \rangle/v_*$ (solid) and velocity dispersion, σ/v_* (dashed) for shock velocities of $\beta = v_s/c = 0.01, 0.03$ and 0.1 . Time is in units of the stellar light crossing time R_*/c with a conversion to hours for our fiducial stellar radius at the top. The line peak and mean velocity are both blue shifted. Higher shock speeds reduce the mean velocity and velocity dispersion but have little effect on the velocity of the peak unless the shock velocity is still higher than the velocities shown here.

line of sight to the star ($\theta = 0$). The observed radius of a shell expanding at velocity v and observed at time t_o is

$$R(v) = \frac{R_* + vt_o}{1 + v(1 - \cos\theta)/c}, \quad (10)$$

where an observer first receives emission from the surface at time $(R_*/c)(1 - \cos\theta)$. This must be accounted for when $t_o < 2R_*/c$. To compute the evolution of the recombination rates, one can either integrate between $R_s = R(v_s)$ and $R_{bo} = R(c)$, or, the problem can be expressed in parabolic coordinates, one of which simply corresponds to the time delay (see Appendix A). For a decelerating shock, a reasonable approximation is to use $v_s = (R_s - R_*)/t = \langle v \rangle$, neglecting any velocity changes over the time R_s/c it takes light to cross the shock.

In particular, for a constant shock velocity, the integrals can be done analytically to yield

$$\frac{\Gamma(t)}{\Gamma_\infty} = \left[1 - \frac{v_{s0}}{c} \right] \left[\frac{R_*}{R_* + v_{s0}t} \right] \left[\frac{t^2}{4t_*(t + t_*)} \right] \quad (11)$$

for $t < 2t_*$ and

$$\frac{\Gamma(t)}{\Gamma_\infty} = \left[1 - \frac{v_{s0}}{c} \right] \left[\frac{R_*}{R_* + v_{s0}t} \right] \left[\frac{t - t_*}{t + t_*} \right] \quad (12)$$

for $t > 2t_*$. The light curve peak now occurs at

$$t_{peak} = \frac{R_*}{\sqrt{cv_{s0}}} \left[\sqrt{2} \left(1 + \frac{v_{s0}}{c} \right)^{1/2} + \left(\frac{v_{s0}}{c} \right)^{1/2} \right] \simeq \frac{\sqrt{2}R_*}{\sqrt{cv_s}}. \quad (13)$$

Adding the time delays smooths and delays the peak of the emission. The peak recombination rate, which has no useful analytic form, drops to $\Gamma_{peak}/\Gamma_\infty = 0.72, 0.64$ and 0.55 for

$v_{s0} = 5000, 10000$ and 20000 km/s, and the time of the peak lengths to $t_{peak} = 12.0, 8.9$ and $6.7t_*$.

These results ignore any shadowing effects of the expanding shock. If we shadow the region with a projected radius of R_s behind the shock, the factor of $1 - R_s/R_{bo}$ in Equation 2 is replaced by

$$\frac{1}{2} \left[1 - \frac{R_s}{R_{bo}} + \frac{1}{2} \cos^{-1} \frac{R_s}{R_{bo}} - \frac{1}{2} \frac{R_s}{R_{bo}} \left(1 - \frac{R_s^2}{R_{bo}^2} \right)^{1/2} \right]. \quad (14)$$

This does not include the effects of light travel times to the observer. When $R_{bo} \rightarrow R_s$, exactly half the emission is shadowed and the factor equals $1/2$. It then increases to $(4 + \pi)/8 \simeq 0.89$ as $R_s/R_{bo} \rightarrow 0$. In practice, shadowing does not play an important role in the evolution of the line flux except at very early times. For example, for $R_* = 1000R_\odot$ and $v_s = 10^4$ km/s, the factor changes by only 3% (0.861 to 0.889) between 0.1 and 10 days. For $R_* = 4000R_\odot$, it changes by 11% (0.798 to 0.888), mostly over the first few hours. Shadowing is important for the shape of the line profiles, as we discuss in §3.

This analysis shows that the time of the peak emission (Equation 13) should be a good measure of the radius of the progenitor star. There is a weak dependence on the shock velocity, but this can be constrained either by spectra of the shocked emission or the initial photospheric expansion rate. This assumes that the tracer is fully ionized at the time of the peak, which will generally be true of hydrogen (see below). The observed peak recombination rate is somewhat lower than for the fully ionized wind, but estimates of the wind density, $\dot{M} \propto (\Gamma_\infty/\Gamma_{peak})^{1/2}$, will be little affected given other uncertainties.

This brings us to the location of the CSM around iPTF13dqy. Yaron et al. (2017) use a size of roughly $1900R_\odot$, significantly larger than the expected radius of a red supergiant. For an effective temperature of $T = 3500T_{35}$ K, the stellar radius is $R_* = 860L_5^{1/2}T_{35}^{-1/2}R_\odot$ for a luminosity of $L = 10^5L_5L_\odot$, quite consistent with our fiducial model. Figure 1 shows the evolution of the recombination rate including light travel times but ignoring shadowing (i.e., Equations 11 and 12) as a function of R_* for a fixed shock velocity of $v_{s0} = 10^4$ km/s. We compare to the observed H α emission from iPTF13dqy, normalizing the model using an unweighted fit to the H α measurements. The rise time of the H α emission is far too slow for the star in our fiducial model. In fact, the rise time is so slow, that it requires an object with $R_* \simeq 4000R_\odot$, even larger than used by Yaron et al. (2017). This result is quite robust against changes in the shock velocity, increasing by 33% if we double the shock velocity and decreasing by 26% if we halve the shock velocity. The dense material surrounding iPTF13dqy had to have been in a shell rather than in a wind extending from the surface of the star.

Yaron et al. (2017) mention the possibility of moving the inner edge of the wind off the surface of the star to make a shell, but do not consider it in any detail. Figure 2 shows the consequences of changing the geometry of the wind. The wind is now a shell extending from either R_* or $5R_*$ to either $10R_*$ or $100R_*$. The case of a wind extending from R_* to $100R_*$ is fairly similar to an infinite wind. With our fiducial $R_* = 821R_\odot$, an inner edge of $5R_* \simeq 4100R_\odot$ reproduces the rise of the light curve well, as we would expect from

Figure 1. Truncating the wind at $10R_*$ cannot reproduce the late time H α flux. However, $10R_* \simeq 6 \times 10^{14}$ cm is the scale on which Yaron et al. (2017) propose to truncate the wind, and $100R_* \simeq 6 \times 10^{15}$ cm is the scale on which Yaron et al. (2017) argue the wind density must be far lower than closer to the star.

It is clear, however, that the dropping production rate of ionizing photons must also play a role since the higher ionization potential lines seen in iPTF13dqy evolve more rapidly than the lower ones. As the emission rate $Q(t)$ of ionizing photons drops, there are eventually too few to balance recombination in the wind. Since the wind is densest close to the shock, we can model this by assuming a fully ionized region extending from the shock to the radius where the integrated recombination rate equals $Q(t)$. As this radius retreats, previously ionized material simply begins to recombine. Additionally, material newly photoionized by the still expanding shell of radiation from the shock break out begins to recombine immediately afterwards. Thus, we need to find the radius $R_{pi}(t)$ where recombination balances ionization,

$$Q(t, E_i) = X\Gamma_\infty \frac{R_*}{R_s(t)} \left(1 - \frac{R_s(t)}{R_{pi}(t)} \right). \quad (15)$$

This depends on the abundance (by number) of the atom X and the ionization energy E_i of interest. A more detailed calculation should also consider the material between the photosphere and the shock front.

We use $X = 1, 0.1$ and 5.4×10^{-4} for hydrogen, helium and oxygen, respectively. Using $X = 1$ for hydrogen, and simply scaling Equation 15 with X corresponds to the assumption that all the available electrons are associated with the ionization of hydrogen and that hydrogen remains fully ionized until helium and oxygen are effectively neutral. These simplifications are quite reasonable. We considered ionization energies of 13.6 eV (hydrogen), 24.6 eV (HeI ionization) 54.4 eV (HeII and OIII ionization), 77.4 eV (OIV ionization) and 113.9 eV (OV ionization). Note that because the HeII and OIII ionization energies are so similar, we should use $X = 0.1$ for helium in both cases.

We estimate $Q(t)$ using a simple model for the evolution of the estimated black body temperature, photospheric radius and luminosity for iPTF13dqy from Yaron et al. (2017). Using a black body spectrum likely overestimates the number of ionizing photons for a given effective temperature but seems adequate for this exploration. We find that the temperature of iPTF13dqy is well-approximated by

$$T_{BB}(t) \simeq 2500 + 6940 \left(\frac{10 \text{ days}}{t} \right)^{1/2} \text{ K} \quad (16)$$

and the photospheric radius is well-approximated by

$$R_{BB}(t) \simeq 10^{13.62} + 10^{15.24} \frac{t}{t + 10 \text{ days}} \text{ cm}. \quad (17)$$

The largest discrepancy is for the first epoch at 4 hours which could be rectified by slightly adjusting the time zero point. However, the exact properties at this epoch are not crucial to our discussion. Note that the derivative of $R_{BB}(t)$ is not expected to be a good estimate of the shock velocity, so there is no need to reconcile this empirical fit with Equation 8. The luminosity is simply $L = 4\pi\sigma R_{BB}^2 T_{BB}^4$. This allows us to compute the evolving number of photoionizing photons above energy E_i ,

$$Q(t, E_i) = \frac{15L(t)}{\pi^4 kT(t)} \gamma \left(\frac{E_i}{kT(t)} \right) \quad (18)$$

where

$$\gamma(u) = \int_u^\infty duu^2 (e^u - 1)^{-1}. \quad (19)$$

We can then combine this with Equation 15 to determine $R_{pi}(t)$, and then invert it to determine the time $t_{pi}(R)$ when material at radius R ceases to be fully photoionized.

Figure 3 shows the resulting evolution of R_{pi} for these five cases. Because the number of ionizing photons is dropping exponentially as the photosphere cools, R_{pi} evolves very quickly. Over a very short period it drops from a very large radius to be very close to the shock radius and then asymptotically tracks the expanding shock. For the particular parameters used in Figure 3, it is no longer possible to ionize HeII, OIII, OIV or OVI after roughly 12 hours. After three days it is no longer possible to ionize HeI, and after roughly 30 days it is no longer possible to ionize HI. This is in qualitative agreement with the spectral evolution found by Yaron et al. (2017), where the oxygen emission lines vanish in less than a day while the H α emission persists.

Given $t_{pi}(R)$, we can then estimate the declining recombination rate given the recombination time of

$$t_r = \frac{4\pi v_w m_p R^2}{\alpha \dot{M}} = 0.019 \frac{v_w 2 R_3^2}{\alpha_{13} \dot{M}_4} \text{ days}. \quad (20)$$

This is also shown in Figure 3 for our standard parameters. If the recombination time is short compared to the present time, the recombination rate will drop rapidly, and *vice versa*. If $\Delta t = t - t_{pi}(R)$ is the time since photoionization ceased, the recombination rate of helium and oxygen declines as $\exp(-\Delta t/t_r)$ while that of hydrogen declines as $(1 + \Delta t/t_r)^2$. The difference arises from the assumption that the electrons are all associated with hydrogen, so that the recombination time at any radius is constant for helium and oxygen but steadily becomes longer as the hydrogen ionization fraction drops. For the final calculations, we combine this model for the effects of the declining numbers of ionizing photons and Equation 8 for the expansion of the shock with Equation A1 to include the effects of the propagation delays.

Figure 4 shows the fiducial model for the recombination rates to OV, OVI, OIII/HeII, HeI and H. The outer envelope is the same as for Figure 1 but for a shock that is slowing down as it expands. When the production rate of the necessary ionizing photons drops below that needed to ionize the wind outside the shock front, the material which has the shortest recombination times recombines first, leading to a rapid initial drop in the recombination rates followed by a tail produced by material with longer recombination times and the continuing photoionization of new material by the still expanding radiation front. Like the H α comparison in Figure 1, everything occurs earlier in this fiducial model than was observed for iPTF13dqy – the evolution of all the lines requires that the material dominating the emission is detached from the stellar surface.

3 RADIATIVE ACCELERATION: BROAD LINE WINGS WITHOUT THOMSON SCATTERING

Yaron et al. (2017) argue that an eruption is needed to produce a CSM dense enough to explain the broad wings of the narrow emission lines seen for the first several days using Thomson scattering. Here we note that radiative acceleration of the wind by the shock break out pulse from an RSG will also naturally produce such line profiles independent of the wind density. The break out radiation has energy E_{bo} and hence momentum E_{bo}/c . For a Thomson optically thin wind, an electron at radius R will capture $E_{bo}\sigma_T/4\pi cR^2$ of this momentum. For a Solar ratio of hydrogen and helium, the mean mass per electron is αm_p with $\alpha = 1.17$, leading to a velocity of $E_{bo}\sigma_T/4\pi c\alpha m_p R^2$. We can safely assume that the medium is ionized because photoionization cross sections are much larger than Thomson and recombination rates are much slower than Thomson scattering rates. After the break out radiation pulse has passed, a wind starting with constant velocity v_w now has the velocity profile

$$v(r) = v_w + v_* \left(\frac{R_*}{r} \right)^2 \quad (21)$$

scaled to the velocity v_* at the stellar surface. This will trigger a hydrodynamic response, but we can view the velocity profile as fixed for the short period of time we consider here. That radiative acceleration produces such velocity profiles has been considered previously, but always in the context of line profiles modified by Thomson scattering in Type II SNe at much later times (e.g., Chugai 2001, or Huang & Chevalier 2018 more recently). There seems not to have been a discussion of this radiative acceleration effect on the recombination line profiles independent of the Thomson optical depth (it may implicitly be included in Chugai (2001), but the focus is on the Thomson scattering). It certainly has not been considered in these early phases where light travel times are also relevant.

Using the $n = 3/2$ results from Matzner & McKee (1999), the break out energy is roughly

$$E_{bo} \simeq 6\kappa_e^{-0.87} \hat{\rho}^{-0.086} E_{51}^{0.56} M_{e10}^{-0.44} R_3^{1.74} \times 10^{48} \text{ erg} \quad (22)$$

where κ_e is the opacity in units of $0.34 \text{ cm}^2/\text{g}$ (i.e., Thomson), $\hat{\rho}^{-0.086} \simeq 1$, and the remaining quantities were defined in §2. This sets a velocity scale of

$$\begin{aligned} v_* &= \frac{E_{bo}\sigma_T}{4\pi c\alpha m_p R_*^2} \\ &\simeq 11000\kappa_e^{-0.87} \hat{\rho}^{-0.086} E_{51}^{0.56} M_{e,10}^{-0.41} R_{*3}^{-0.26} \text{ km/s}, \end{aligned} \quad (23)$$

which is remarkably high. The acceleration period lasts roughly an hour for a red supergiant, and we ignore this initial transient phase. Since the SN shock is essentially expanding at close to v_* , the temporal window for seeing velocities close to v_* is short.

Given the velocity profile established by the radiative acceleration, and the observed (i.e., including time delays) locations of the shock and the radiation pulse (Equation 10), we can compute the expected shape of the emission line profile as a function of time. Here we include the shadowing of the CSM by the expanding shock, as this has significant effects on the line shapes. Figure 5 shows the evolution of the line peak, v_p , the mean velocity, $\langle v \rangle$, and the dispersion

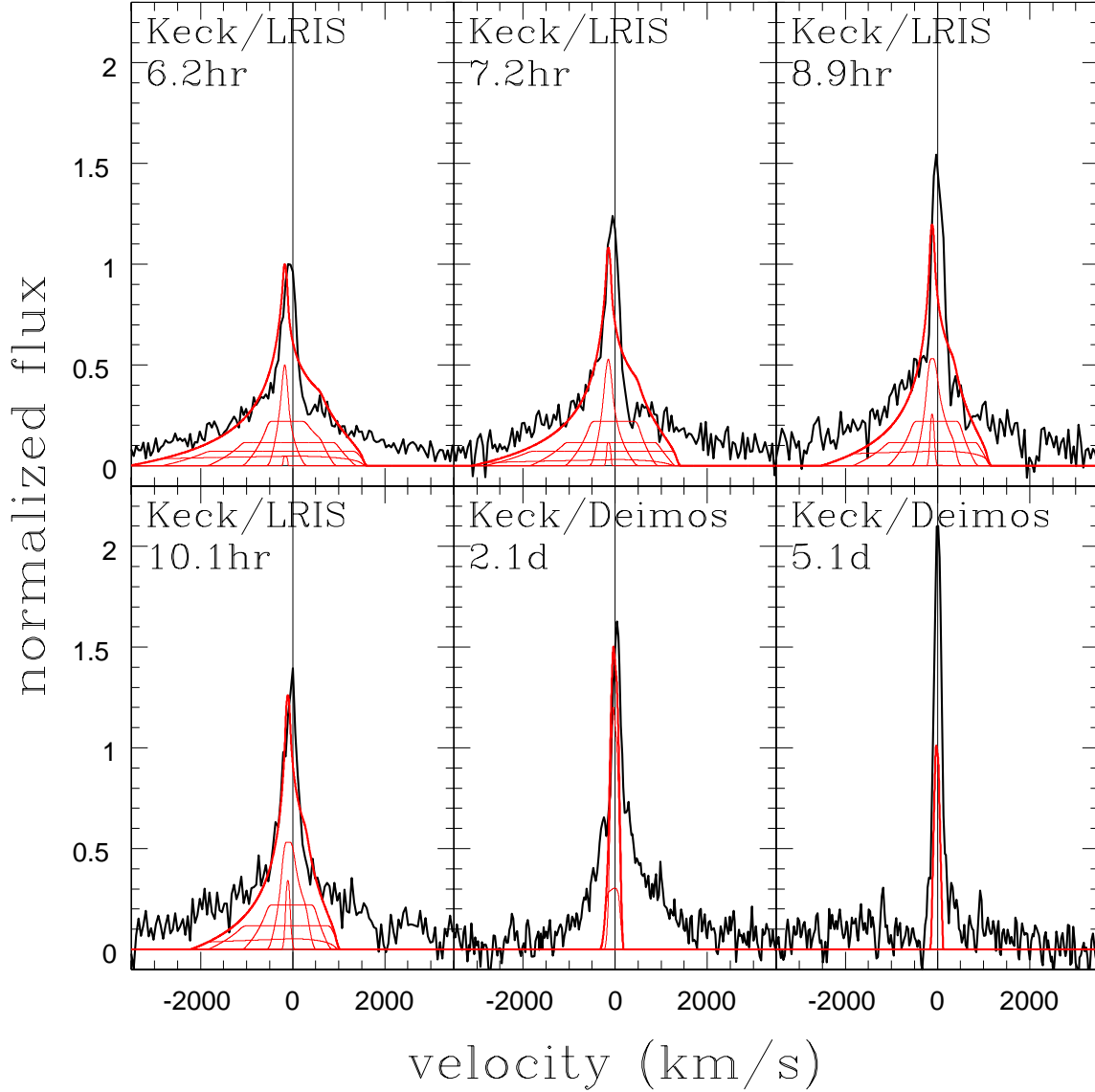


Figure 6. The H α emission line (black curves) of iPTF13dqy in velocity space with the flux normalized to a peak of unity in the first epoch (upper left) and then following its evolution to 8.8 days. The heavy red curve shows a radiative acceleration plus recombination model for the evolution of the line for a $\rho \propto 1/r^2$ wind extending from R_* to $10^4 R_*$. The light solid lines show the contributions from radial regions of 1.67-2, 2-2.5, 2.5-3.33, 3.33-5, 5-10 and 10- $10^4 R_*$ around the star, defined so that the recombination line fluxes of each region when fully ionized equal 10% of the flux of a fully ionized wind extending from the star's surface. Regions closer to the star have broader velocity profiles. Regions make no contribution when either fully inside the observed shock radius or outside the expanding photoionized region. Time delays and shadowing of the CSM by the expanding shock are included and lead to the line asymmetries. The velocity is the width of the top hat used to model instrumental resolutions.

in velocity, σ , for a wind speed $v_w = 0$. The velocities are scaled by v_* , and both the line peak and the mean velocity are blue shifted. If we measure time in units of the stellar light crossing time, ct/R_* , the profiles depend only the shock speed relative to the speed of light, $\beta = v_s/c$, and we show results for $\beta = 0.01, 0.03$, and 0.1 . The mean and the dispersion in velocity decrease as the shock speed increases because the fastest moving parts of the CSM are shocked earlier. The Doppler shift of the line peak is nearly independent of β . Figure 5 also shows the conversion to hours assuming our fiducial stellar radius. For a decelerating shock,

Figure 5 can be interpreted using the mean shock velocity, $\beta = (R_s(t) - R_*)/ct = \langle v \rangle/c$. This (safely) ignores deceleration of the shock on a light crossing time.

Figure 6 shows the expected line evolution for a constant velocity wind extending from R_* to $10^4 R_*$ with $R_* = 821 R_\odot$, $v_w = 76$ km/s, $v_s = 20000$ km/s and $v_* \simeq 11000$ km/s based on Eqn. 24. The times are chosen to match the Keck spectroscopic observations of iPTF13dqy by Yaron et al. (2017). They are smoothed with a 100 km/s top hat to approximate the effects of finite spectral resolution, and normalized to a peak of unity in the first epoch.

To illustrate the regions responsible for the line shape, we show the contributions from radial regions that when fully ionized will produce 10% of the recombination radiation of a fully ionized wind. The chosen annuli are 1.67-2, 2-2.5, 2.5-3.33, 3.33-5, 5-10 and 10-10⁴ R_* . Regions closer to the star are swept over by the shock very quickly and have such broad velocity widths that they would be very difficult to separate from the continuum emission.

At the earliest epoch, the line flux is dominated by very broad wings from regions close to the star, with little contribution from the outermost annulus. The narrow peak is blue-shifted because the most redshifted material is shadowed by the shock and because of the near/far asymmetry in the observed photoionized region (Eqn. 10). This also leads to a line asymmetry with more blue than red flux at higher velocities. The lines narrow and the blue shifts diminish as the shock passes over the most accelerated material and the photoionization front reaches larger radii. The peak recombination flux, as discussed in §2, occurs at intermediate times. Note that these line profiles are independent of the Thomson optical depth of the CSM, they are purely due to the radiative acceleration.

For comparison, we show the spectra of the H α region from Yaron et al. (2017). We obtained the spectra of iPTF13dqy from the WISerEP (Yaron & Gal-Yam 2012) repository. We corrected for redshift, using the line center in the Keck/Deimos 5.1 day spectrum to define zero velocity. The mean fluxes in windows adjacent to the line were used to subtract a linear continuum. These windows are sufficiently far removed from the line center that they should be little contaminated even by very broad line wings. This model for the continuum works reasonably well, although there are several epochs where the continuum is not very flat.

The models qualitatively reproduce the evolution of the spectra even though we made no adjustments to the parameters. The observed line profiles are somewhat less asymmetric and the early-time peaks are less blue-shifted ($\simeq 80$ km/s versus $\simeq 150$ km/s at 6.2 hr), and either a larger v_* or a lower v_s would help to keep the lines broader for longer. Allowing the shock to decelerate would also keep the lines broader for a longer period of time. One could also increase v_* while having less material near the star, a solution suggested by the slow rise time of the H α emission. Since in §4 we will propose a very different explanation and more geometrically complex solution, we did not attempt to optimize the model.

Many of these effects would have a similar effect on the line profiles produced by Thomson scattering. For example, the optical depth is largest, and so the scattering wings broadest, at early times. The near/far asymmetry produced by the time delays and the shadowing by the shock would again produce blue/red asymmetries in the line profiles. The Thomson optical depth of the CSM will scale as $\tau_0 R_*/R_s$ where R_s is the shock radius, and the scattering wings will have a width $\sim v_e \tau$ assuming a random walk in velocity space (i.e., $N \sim \tau^2$ scatterings) with $v_e \simeq 10^3$ km/s for electrons with $T \simeq 20000$ K. The optical depth changes little over the first four epochs, dropping by only 20% between 6.2 and 10.1 hours for our fiducial parameters, but then falling rapidly to 0.24 τ_0 and 0.11 τ_0 by 2.1 and 5.2 days. As the optical depth drops, the lines become narrower.

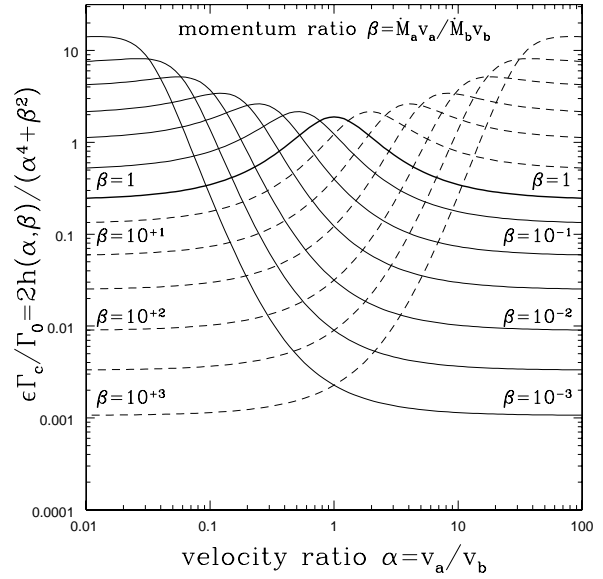


Figure 7. The efficiency factor Γ_c/Γ_b from Equation 33 as a function of the relative wind speeds $\alpha = v_a/v_b$ for a range of wind momentum ratios $\beta = \dot{M}_a v_a / \dot{M}_b v_b$ for recombination in a thin shock created by colliding winds relative to recombination in the winds of the binaries starting at a radius equal to the binary separation.

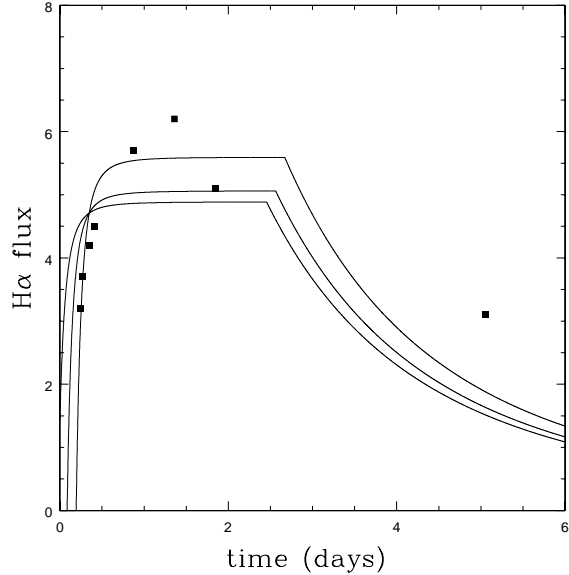


Figure 8. The recombination light curves for a $\beta = 1$ colliding wind with $D/2 = 4000R_\odot$, $R_* = 821R_\odot$ and $v_{s0} = 10^4$ km/s. The three curves correspond to putting the secondary along the line of sight to the primary (fastest rise), perpendicular to the line of sight (middle) and on the far side of the primary (slowest rise). No other light travel time effects are included. The points are the observed H α light curve from Yaron et al. (2017), and the curves are normalized to fit the equally weighted observations.

4 A COLLIDING WIND

If we take the LBT and X-ray evidence at face value, RSGs do not have pre-SN outbursts, so we require an alternate explanation. While radiative acceleration can naturally explain the broad line wings without the need for a medium optically thick to Thomson scattering, the recombination flux (Equation 2) still requires a high density CSM. To avoid the need for a pre-SN eruption, we need a mechanism to increase the recombination rate given a mass loss rate normally associated with an RSG. This requires a means of producing a denser medium than expected for such a wind, with a shell-like structure to explain the rise time and the lack of radio/X-ray emission at late times.

We expect a large fraction of SNe to occur in binaries, where the binary companion will typically be a hotter, main sequence star (see, e.g., Kochanek 2009). Such stars have relatively low \dot{M} , high velocity winds, so photoionizing the wind of the secondary also cannot produce the observed line fluxes. However, the secondary also modifies the winds. In particular, there is a shocked boundary layer created by the collision of the winds from the two stars. In many Wolf-Rayet binaries, the shocked material cools to the point of dust formation (e.g., Tuthill et al. 1999 Monnier et al. 1999, Monnier et al. 2002, Dougherty et al. 2005, Tuthill et al. 2008, Williams et al. 2009), which means that the density must far exceed the density a wind would have at such a distance from an isolated star. Since recombination is a n^2 process, this can greatly enhance the recombination rate over expectations for a smoothly expanding wind in the same way that clumping in stellar winds can significantly enhances line strengths for a given mass loss rate (e.g., Puls et al. 2008). While we focus on colliding winds because there is an elegant analytic model, hot secondaries can produce similar effects without any wind because of the HII region that they form in the wind of the primary (see the α Sco models of Braun et al. 2012 and the short discussion in Appendix B).

Canto et al. (1996) present an analytic solution for the geometry and surface density of an axisymmetric colliding wind based on mass and momentum conservation and assuming that efficient cooling makes the shocked region “infinitely” thin. Star a (the primary) is at the origin and star b (the secondary) lies at a distance D along the z axis. Relative to star a geometry provides the relation

$$R(\theta_a) = D \sin \theta_b \csc(\theta_a + \theta_b) = Df(\theta_a) \quad (24)$$

where θ_a is a spherical polar angle centered on star a with $\theta_a = 0$ pointing to star b and θ_b is a spherical polar angle centered on star b with $\theta_b = 0$ pointing to star a. Mass and momentum conservation lead to the constraint that

$$\theta_b \cot \theta_b = 1 + \beta(\theta_a \cot \theta_a - 1) \quad (25)$$

where $\beta = \dot{M}_a v_a / \dot{M}_b v_b$ is the ratio of the wind momenta. The surface density in the shock is then $\sigma(\theta_a) = \sigma_0 g(\theta_a)$ where $\sigma_0 = \dot{M}_a / 2\pi\beta v_a D$, and $g(\theta_a) = A/B$ with

$$\begin{aligned} A &= \sin(\theta_a + \theta_b) \csc \theta_a \csc \theta_b \times \\ &\quad [\beta(1 - \cos \theta_a) + \alpha(1 - \cos \theta_b)]^2, \\ B^2 &= [\beta(\theta_a - \sin \theta_a \cos \theta_a) + (\theta_b - \sin \theta_b \cos \theta_b)]^2 + \\ &\quad [\beta \sin^2 \theta_a - \sin^2 \theta_b]^2 \end{aligned} \quad (26)$$

and $\alpha = v_a/v_b$.

We can estimate the recombination rate associated with the wind interface as follows. First, we assume that the layer has constant fractional thickness, $\Delta = \epsilon R(\theta_a) = \epsilon Df(\theta_a)$, relative to the distance from the primary. This makes the gas density $\rho = \sigma_0 g(\theta_a)/\Delta$. We also need the area element of the shock surface,

$$dA = 2\pi D^2 f(\theta_a) \sin(\theta_a) \left[f(\theta_a)^2 + \left(\frac{df(\theta_a)}{d\theta_a} \right)^2 \right]^{1/2} d\theta_a. \quad (27)$$

The recombination rate per unit area is $\alpha_R \rho^2 / \mu^2 m_p^2 \Delta$, and the total is

$$\Gamma_c = \frac{2\pi\alpha_R\sigma_0^2 D}{\epsilon\mu^2 m_p^2} h(\alpha, \beta) \quad (28)$$

where

$$h(\alpha, \beta) = \int d\theta_a \frac{\epsilon D g^2(\theta_a) f(\theta_a) \sin(\theta_a)}{\Delta} \left[f^2 + \left(\frac{df}{d\theta_a} \right)^2 \right]^{1/2} \quad (29)$$

which for our assumed scaling of the thickness is

$$h(\alpha, \beta) = \int d\theta_a g^2(\theta_a) \sin(\theta_a) \left[f^2 + \left(\frac{df}{d\theta_a} \right)^2 \right]^{\alpha/2}. \quad (30)$$

For winds of equal momentum ($\beta \equiv 1$), this becomes

$$h(\alpha, \beta \equiv 1) = 16(1 + \alpha)^4 \int d\theta_a \frac{\sin^6(\theta_a/2) \tan(\theta_a/2)}{(2\theta_a - \sin \theta_a)^2} \quad (31)$$

which is $h(\alpha, \beta \equiv 1) \simeq 0.12(1 + \alpha)^4$ when integrated over the full shock ($0 \leq \theta_1 \leq \pi/2$).

The overall scale can be made clearer by normalizing the recombination rate to the rate which would be produced by the two stellar winds starting from a radius equal to the binary separation D ,

$$\Gamma_D = \frac{\alpha_R}{4\pi\mu^2 m_p^2 D} \left(\frac{\dot{M}_a^2}{v_a^2} + \frac{\dot{M}_b^2}{v_b^2} \right). \quad (32)$$

This is less than the rate for an individual star of radius R_* (Equation 1) by D/R_* . Given this scaling, the recombination rate from the wind collision region becomes

$$\Gamma_c = \epsilon^{-1} \Gamma_D \frac{2h(\alpha, \beta)}{\alpha^4 + \beta^2}. \quad (33)$$

This function is shown in Figure 7. As required, the result is unchanged if the labels of the two stars are reversed ($\alpha \rightarrow \alpha^{-1}$ and $\beta \rightarrow \beta^{-1}$). For equal momentum winds ($\beta \equiv 1$) this becomes

$$\Gamma_c = \frac{8\alpha_R(1 + \alpha)^4 \dot{M}_a^2}{\epsilon\pi D\mu^2 m_p^2 v_a^2} \int d\theta_a \frac{\sin^6(\theta_a/2) \tan(\theta_a/2)}{(2\theta_a - \sin \theta_a)^2} \quad (34)$$

which when integrated over the shock is

$$\Gamma_c \simeq \frac{0.29(1 + \alpha)^4}{\epsilon} \left[\frac{\alpha_R \dot{M}_a^2}{4\pi v_w^2 \mu^2 m_p^2 D} \right] \quad (35)$$

where the term in brackets is the same as in Equation 1 for a star of radius D .

If we now equate this to the peak H α flux (see §2), then

$$\dot{M}_a \simeq 3.5v_a 2\epsilon^{1/2} D_4^{1/2} \alpha_{H\alpha 13}^{-1/2} \times 10^{-3} M_\odot/\text{year} \quad (36)$$

where $D = 10^4 D_4 R_\odot$ places the shock at the right distance to explain the rise time of the line fluxes, the H α

rate is scaled to $\alpha_{H\alpha} = 10^{-13} \alpha_{H\alpha 13} \text{ cm}^3/\text{s}$ corresponding to a temperature of roughly 10^4 K (e.g., Draine 2011), and we have assumed that the primary is a red giant with a slow wind ($v_a = 100v_{a2} \text{ km/s}$) and the secondary is a hot main sequence star with a lower mass loss rate ($\dot{M} \sim 10^{-10} M_\odot/\text{year}$) but a very high wind velocity ($v_b \simeq 10^3 \text{ km/s}$). This means that the RSG wind has far more momentum and we have $\beta \simeq 100$ and $\alpha \simeq 10^{-2}$. Examining Figure 7, we see that this reduces the dimensionless factor in Equation 28 by a factor of 20 and so requires an increase in the mass loss rate of a factor of 4-5 to get the same recombination rate.

Finally, we assume that the shock collision region cools as it does in the colliding wind Wolf-Rayet binaries. The surface density at the stagnation point (the position of the interface on the axis separating the stars) is $\sigma_s = 3(1 + \alpha)^2 \beta^{1/2} \sigma_0/8$, so the density is

$$\rho_s = \frac{3(1 + \alpha)^2 (1 + \beta^{1/2}) \dot{M}_a}{16\pi\epsilon\beta v_a D^2}. \quad (37)$$

Equating the pressure in the layer $\rho_s kT/\mu m_p$ to the incoming ram pressure from the RSG we find that

$$\epsilon = \frac{3(1 + \alpha)^2}{2(1 + \beta^{1/2})} \frac{kT}{\mu m_p v_a^2} \simeq 0.06 \mu^{-1} v_{10}^{-2} T_3 \quad (38)$$

for $\beta = 1$ and $\alpha \simeq 0$ with the pre-factor dropping to 0.01 for $\beta = 10^2$ and $\alpha \simeq 0$ so that

$$\dot{M}_a \sim D_4^{1/2} T_3^{1/2} \alpha_{H\alpha 13}^{1/2} \times 10^{-4} M_\odot/\text{year}. \quad (39)$$

While still high, this is now in the regime of RSG winds and largely avoids the late-time emission limits from Yaron et al. (2017). The required \dot{M} can be driven downwards by including the photoionization of the winds of the primary by the secondary (Appendix B), which should be similar to making β closer to unity, or by scaling the thickness Δ of the interface with radius more slowly than as a constant fraction of the radius.

5 DISCUSSION

In this paper we introduce three general points about flash spectroscopy and the potential effects of binarity on interpretations of flash spectroscopy. The first general point (§2) is that the time-dependent flux of the low ionization lines determines the size of the star. In particular, the flux peaks at $t_{peak} \simeq R_* \sqrt{2/cv_{s0}}$ (Eqn. 13) where R_* is the stellar radius and v_{s0} is the shock speed. The time t_{peak} is a trade off between the outgoing radiation pulse from the shock break out ionizing more material and the outgoing shock front running over the ionized material. The decreasing temperature of the radiation field eventually cuts off the line emission, with the emission from high ionization energy lines being cut off earlier than low ionization energy lines. This means that the hydrogen Balmer lines will be the best probes of the size of the emission region.

The second general point (§3) is that flash spectroscopy observations should always find broad line wings at early times. For Type II SNe with giant progenitors, radiative acceleration produces broad wings independent of the Thomson optical depth of the CSM. For stripped envelope SNe, radiative acceleration is much less effective because far

less energy is associated with the shock break out (e.g., Matzner & McKee 1999), but the line-accelerated winds expected for the progenitors of stripped envelope SNe will intrinsically possess broad wings. Detection of broad wings in flash spectroscopy of Type II SNe are thus a test of the predicted energetics of shock break out radiation. Since the velocity profile created by radiative acceleration is $\propto r^{-2}$, the lines will narrow quite rapidly as the shock front runs over the fastest material.

The third general point (§4) is that many SN occur in binary systems (e.g., Kochanek 2009) and binaries sculpt the winds of the primary through both their winds and their production of ionizing radiation. In particular, the winds from the two stars collide, producing a boundary layer separating the two winds (e.g., Canto et al. 1996). The shock collision regions are directly observed in some Wolf-Rayet binaries (e.g., Monnier et al. 1999, Monnier et al. 2002, Dougherty et al. 2005, Tuthill et al. 2008, Williams et al. 2009). More importantly, these systems form dust, which means that the gas must cool to produce a very dense, cold layer, shielded from the harsh radiation environment produced by the Wolf-Rayet stars. Cooling in the shock provides a source of high density material that can produce flash spectroscopy recombination rates that neither star could produce in isolation. It is likely that the sculpting of the CSM by the winds and photoionizing fluxes of secondary companions explains many of the deviations seen in X-ray (e.g., Dwarkadas & Gruszko 2012) or radio (e.g., Margutti et al. 2017 or Chandra 2018) light curves from the expectations for a simple $\rho \propto r^{-2}$ wind. Detailed simulations are needed to follow the fully-developed ‘‘pinwheel’’ shock geometry created by orbital motions (e.g., Stevens et al. 1992, Parkin & Pittard 2008, Lamberts et al. 2011, Lamberts et al. 2012).

We also discuss these effects for the specific example of iPTF13dqy, an otherwise normal Type IIP SNe where Yaron et al. (2017) use their flash spectroscopy results to argue for a short lived, high mass loss rate ($\dot{M} \sim 10^{-3} M_\odot/\text{year}$) pre-SN eruption that produced a dense CSM surrounding the star. We were driven to search for an alternate explanation because at least two lines of evidence indicate that normal Type IIP SNe do not have such eruptions: (1) the absence of such events for 4 normal Type II SNe (Kochanek et al. 2017, Johnson et al. 2017) in the LBT search for failed supernovae (Gerke et al. 2015, Adams et al. 2016) and (2) the absence of X-ray emission from normal Type IIP SNe (e.g., Dwarkadas 2014).

First, the time evolution of iPTF13dqy’s $H\alpha$ light curve requires that the dense CSM starts at $\sim 4000R_\odot$ and so must be detached from the star. Moreover, the continued $H\alpha$ emission after ~ 5 days requires that the dense CSM extends to the radial scales where Yaron et al. (2017) propose that it is truncated. Second, the broad line wings are created by radiative acceleration and confirm the energy scale of $E_{bo} \sim 10^{40} \text{ erg}$ predicted by theoretical models of shock break outs from RSGs. The broad line wings are not evidence of a CSM optically thick to Thomson scattering. Both the evolution of the line fluxes and the line profiles appear to require a more complicated geometry than a simple wind extending from the stellar surface and the line fluxes still require the existence of a denser CSM than a normal RSG wind. The geometry and the line fluxes are both consistent

with the progenitor having a relatively normal RSG wind which is swept up into a dense, cooling layer by the wind of a secondary to produce a much higher recombination rate than would be expected for an isolated wind. Because the wind densities are much lower than invoked by Yaron et al. (2017) and the geometry of the dense shell (“paraboloidal”) is different from the geometry of the expanding shock (“spherical”), there is no difficulty staying under the later time limits on X-ray or radio emission from the system.

These points also explain the peculiarities of the Type IIb SN iPTF13ast (SN 2013cu, Gal-Yam et al. 2014). Like iPTF13dqy, flash spectroscopy of iPTF13ast showed broad wings which Gal-Yam et al. (2014) interpret as being intrinsic to a pre-SN, fast ($\sim 10^3$ km/s) Wolf-Rayet-like wind because their model of the wind is Thomson optically thin and so cannot produce the wings by scattering. Gal-Yam et al. (2014) cite SN 2008x as an example of a Type IIb with a Wolf-Rayet progenitor (Crockett et al. 2008), but this hypothesis is incompatible with more recent observations (Folatelli et al. 2015). The best-studied progenitors of Type IIb SN are all yellow supergiants (e.g., SN 1993J and SN 2011dh, Aldering et al. 1994, Maund et al. 2011, Van Dyk et al. 2011) which should have far slower wind speeds than Wolf-Rayet stars since stellar wind speeds are generally comparable to stellar escape velocities. Moreover, yellow supergiants are unlikely to have line driven winds because they are too cool (e.g., Lamers & Cassinelli 1999).

For iPTF13ast, we have no information about the rise time of the line emission, although it would be very rapid for a compact progenitor because the star is so small. Radiative acceleration does, however, provide a natural explanation for the broad line wings, obviating the need for a fast pre-existing wind. With the reduced wind speed, the mass loss rates become more reasonable than the $\dot{M} \sim 10^{-2} M_\odot/\text{year}$ implied by the recombination rate and $v_w \sim 10^3$ km/s. Moreover, most models of Type IIb SNe invoke binary mass transfer (e.g., Maund et al. 2004, Benvenuto et al. 2013, Bersten et al. 2014 but see Maund et al. 2015), which can again provide a high density region to boost the recombination rates above those for an isolated star with the same mass loss rate.

ACKNOWLEDGMENTS

CSK thanks S. Johnson, M. Pinsonneault, R. Pogge, A. Piro and T. Thompson for extensive discussions. CSK is supported by NSF grants AST-1515876 and AST-1515927.

APPENDIX A: INCLUDING TIME DELAYS

The effects of light propagation times can be incorporated relatively easily using the parabolic coordinates $x = \sigma\tau \cos\phi$, $y = \sigma\tau \sin\phi$ and $z = (\tau^2 - \sigma^2)/2$. The radius is $r = (\sigma^2 + \tau^2)/2$, and for an observation at time t the light was emitted at time $t - \sigma^2/c$. The volume element is $dV = \sigma\tau(\sigma^2 + \tau^2)d\sigma d\tau d\phi$. The recombination rate of the system compared to that of a fully ionized wind starting at the stellar surface is ($\Gamma = \Gamma_\infty f(t)$)

$$f(t) = \frac{R_*}{4\pi} \int \frac{dV}{r^4} g(r, t) = 8R_* \int \frac{\sigma\tau g(r, t) d\sigma d\tau}{(\sigma^2 + \tau^2)^3} \quad (\text{A1})$$

where $g(r, t)$ represents any time-dependent recombination. The limits of integration are from σ_s to σ_{bo} where $0 = 2R_s(\sigma_s) - \sigma_s^2$ and $0 = 2R_{bo}(\sigma_{bo}) - \sigma_{bo}^2$. For a given σ the limits on τ are from $\tau^2 = \max(0, 2R_s(\sigma) - \sigma^2)$ to $\tau^2 = 2R_{bo}(\sigma) - \sigma^2$.

If there is no additional function $g(r, t)$, the τ integral is analytic in terms of $R_s(t)$ and $R_{bo}(t)$,

$$f(t) = \frac{R_*}{2} \int_0^{\sigma_s} \sigma d\sigma \left(\frac{1}{R_s(\sigma)^2} - \frac{1}{R_{bo}(\sigma)^2} \right) + \frac{R_*}{2} \int_{\sigma_s}^{\sigma_{bo}} d\sigma \left(\frac{4}{\sigma^3} - \frac{\sigma}{R_{bo}(\sigma)^2} \right) \quad (\text{A2})$$

For inner and outer radii expanding at v_s and c , respectively, only the first integral contributes for $t < 2R_*/c$ with $\sigma_s^2 = ct$. At later times, $\sigma_s^2 = 2(R_* + v_s t)/(1 + 2v_s/c)$ and $\sigma_{bo}^2 = 2(R_* + ct)/3$. This provides the analytic solution given in Equations 11 and 13.

APPENDIX B: HII REGIONS FROM SECONDARIES

Hot main sequence stars may have lower momentum winds than RSGs, but they also produce ionizing photons which enhance their ability to perturb the RSG wind by driving the formation of an HII region around the secondary. Outside of Braun et al. (2012), there seems to be no discussion of this physical effect. The natural scale for the ionizing flux from the secondary is ionizing photon production rate needed to fully ionize the primary’s wind,

$$Q_{crit} = \frac{\dot{M}^2 \alpha_R}{4\pi v_w^2 \mu^2 m_p^2 R_*} \simeq 1.7 \mu^{-2} \dot{M}_4^2 \alpha_{13} v_{w10}^{-2} R_{*3}^{-1} \times 10^{51} \text{s}^{-1}. \quad (\text{B1})$$

This means that an 05 (B0) companion produces enough ionizing photons to fully photoionize a wind with $\dot{M} \simeq 10^{-5} M_\odot/\text{year}$ ($10^{-6} M_\odot/\text{year}$). As a toy model, suppose the secondary produces ionizing photons at rate Q and we assume the density distribution along the line from the primary to the secondary is unperturbed by the photoionization. In this case, the radius of the equilibrium photoionization front from the primary is

$$\frac{r}{R_*} = \left[\frac{Q}{Q_{crit}} + \frac{R_*}{D} \right]^{-1} \quad (\text{B2})$$

where D is again the binary separation. For comparison, the stagnation point of the colliding wind shock is at $R_s = D\beta^{1/2}/(1 + \beta^{1/2})$. In short, a hot main sequence companion without a wind can likely perturb the wind from the RSG almost as effectively as one with a fast, low density wind. In practice, both effects will be present.

REFERENCES

- Adams, S. M., Kochanek, C. S., Gerke, J. R., & Stanek, K. Z. 2016, arXiv:1610.02402
- Aldering, G., Humphreys, R. M., & Richmond, M. 1994, AJ, 107, 662
- Benvenuto, O. G., Bersten, M. C., & Nomoto, K. 2013, ApJ, 762, 74

- Bersten, M. C., Benvenuto, O. G., Folatelli, G., et al. 2014, *AJ*, 148, 68
- Braun, K., Baade, R., Reimers, D., & Hagen, H.-J. 2012, *AAP*, 546, A3
- Canto, J., Raga, A. C., & Wilkin, F. P. 1996, *ApJ*, 469, 729
- Chakraborti, S., Ray, A., Smith, R., et al. 2016, *ApJ*, 817, 22
- Chandra, P. 2018, *SSRv*, 214, #27
- Chevalier, R. A. 1982, *ApJ*, 258, 790
- Chevalier, R. A., & Irwin, C. M. 2011, *ApJL*, 729, L6
- Chugai, N. N. 2001, *MNRAS*, 326, 1448
- Crockett, R. M., Eldridge, J. J., Smartt, S. J., et al. 2008, *MNRAS*, 391, L5
- Dougherty, S. M., Beasley, A. J., Claussen, M. J., Zauderer, B. A., & Bolingbroke, N. J. 2005, *ApJ*, 623, 447
- Draine, B. T. 2011, *Physics of the Interstellar and Inter-galactic Medium* by Bruce T. Draine. Princeton University Press, 2011. ISBN: 978-0-691-12214-4,
- Dwarkadas, V. V., & Gruszko, J. 2012, *MNRAS*, 419, 1515
- Dwarkadas, V. V. 2014, *MNRAS*, 440, 1917
- Folatelli, G., Bersten, M. C., Kuncarayakti, H., et al. 2015, *ApJ*, 811, 147
- Fraser, M., Magee, M., Kotak, R., et al. 2013, *ApJL*, 779, L8
- Fuller, J. 2017, arXiv:1704.08696
- Gal-Yam, A. 2012, *Science*, 337, 927
- Yaron, O., & Gal-Yam, A. 2012, *PASP*, 124, 668
- Gal-Yam, A., Arcavi, I., Ofek, E. O., et al. 2014, *Nature*, 509, 471
- Gerke, J. R., Kochanek, C. S., & Stanek, K. Z. 2015, *MNRAS*, 450, 3289
- Gräfener, G., & Vink, J. S. 2016, *MNRAS*, 455, 112
- Groh, J. H. 2014, *AAP*, 572, L11
- Huang, C., & Chevalier, R. A. 2018, *MNRAS*, 475, 1261
- Johnson, S. A., Kochanek, C. S., & Adams, S. M. 2017, arXiv:1712.03957
- Khazov, D., Yaron, O., Gal-Yam, A., et al. 2016, *ApJ*, 818, 3
- Kochanek, C. S. 2009, *ApJ*, 707, 1578
- Kochanek, C. S. 2011, *ApJ*, 743, 73
- Kochanek, C. S., Fraser, M., Adams, S. M., et al. 2017, *MNRAS*, 467, 3347
- Lamberts, A., Fromang, S., & Dubus, G. 2011, *MNRAS*, 418, 2618
- Lamberts, A., Dubus, G., Lesur, G., & Fromang, S. 2012, *AAP*, 546, A60
- Lamers, H. J. G. L. M., & Cassinelli, J. P. 1999, *Introduction to Stellar Winds*, by Henny J. G. L. M. Lamers and Joseph P. Cassinelli, pp. 452. ISBN 0521593980. Cambridge, UK: Cambridge University Press, June 1999., 452
- Margutti, R., Kamble, A., Milisavljevic, D., et al. 2017, *ApJ*, 835, 140
- Matzner, C. D., & McKee, C. F. 1999, *ApJ*, 510, 379
- Mauerhan, J. C., Smith, N., Filippenko, A. V., et al. 2013, *MNRAS*, 430, 1801
- Maund, J. R., Smartt, S. J., Kudritzki, R. P., Podsiadlowski, P., & Gilmore, G. F. 2004, *Nature*, 427, 129
- Maund, J. R., Fraser, M., Ergon, M., et al. 2011, *ApJL*, 739, L37
- Maund, J. R., Arcavi, I., Ergon, M., et al. 2015, *MNRAS*, 454, 2580
- Monnier, J. D., Tuthill, P. G., & Danchi, W. C. 1999, *ApJL*, 525, L97
- Monnier, J. D., Tuthill, P. G., & Danchi, W. C. 2002, *ApJL*, 567, L137
- Morozova, V., Piro, A. L., & Valenti, S. 2017, *ApJ*, 838, 28
- Morozova, V., Piro, A. L., & Valenti, S. 2018, *ApJ*, 858, 15
- Ofek, E. O., Sullivan, M., Shaviv, N. J., et al. 2014, *ApJ*, 789, 104
- Ofek, E. O., Cenko, S. B., Shaviv, N. J., et al. 2016, arXiv:1605.02450
- Parkin, E. R., & Pittard, J. M. 2008, *MNRAS*, 388, 1047
- Pastorello, A., Smartt, S. J., Mattila, S., et al. 2007, *Nature*, 447, 829
- Puls, J., Vink, J. S., & Najarro, F. 2008, *A&ARv*, 16, 209
- Quataert, E., & Shiode, J. 2012, *MNRAS*, 423, L92
- Shiode, J. H., & Quataert, E. 2014, *ApJ*, 780, 96
- Smith, N. 2014, *ARA&A*, 52, 487
- Smith, N., & Arnett, W. D. 2014, *ApJ*, 785, 82
- Stevens, I. R., Blondin, J. M., & Pollock, A. M. T. 1992, *ApJ*, 386, 265
- Tuthill, P. G., Monnier, J. D., & Danchi, W. C. 1999, *Nature*, 398, 487
- Tuthill, P. G., Monnier, J. D., Lawrance, N., et al. 2008, *ApJ*, 675, 698-710
- Van Dyk, S. D., Li, W., Cenko, S. B., et al. 2011, *ApJL*, 741, L28
- Williams, P. M., Marchenko, S. V., Marston, A. P., et al. 2009, *MNRAS*, 395, 1749
- Woosley, S. E., Heger, A., & Weaver, T. A. 2002, *Reviews of Modern Physics*, 74, 1015
- Woosley, S. E., & Heger, A. 2015, *ApJ*, 810, 34
- Yaron, O., Perley, D. A., Gal-Yam, A., et al. 2017, arXiv:1701.02596